Materials Advances

ROYAL SOCIETY OF CHEMISTRY

PAPER

View Article Online
View Journal | View Issue

Cite this: *Mater. Adv.*, 2024, 5, 1106

Synthesis of Quasi-MOFs featuring special hub-and-spoke channels and surface NiO species for enhanced total hydrogenation of furfural†

Qiuju Fu,[ab] Liting Yan,[a] Lingzhi Yang,*[c] Dandan Liu,[b] Shuo Zhang,[b] Huimin Jiang,[b] Wenpeng Xie,[b] Haiyan Wang*[d] and Xuebo Zhao*[ab]

Received 31st October 2023,
Accepted 1st December 2023

DOI: 10.1039/d3ma00938f

rsc.li/materials-advances

The design of Ni-based catalysts with high activity for the conversion of furfural (FFR) into tetrahydrofurfuryl alcohol (THFA) holds great promise for the upgrading of renewable resources. However, the weak affinity between the furan ring and Ni^0 limits the hydrogenation reaction under moderate conditions. In this work, we propose a new strategy for the design of highly efficient hydrogenation catalysts. Quasi-MOFs with unique hub-and-spoke channels, and abundant Ni^0 and surface NiO species were successfully prepared through controlled deligandation of Ni-MOF-74 by partial thermal transformation. The spokewise channels facilitate the delivery of the reactants and expose more catalytic active sites. The obtained Quasi-MOF exhibits strong interaction between Ni metal nanoparticles and the partially decomposed ligand. The presence of surface NiO species can strengthen the affinity between the catalyst and FFR/H_2 molecules and enhance the H-donation capacity, leading to dramatically enhanced hydrogenation activity. The synthesized Quasi-MOF-9h exhibited excellent activity in the total hydrogenation of FFR, achieving 98% yield of THFA within 4 h at 70 °C and 3 MPa H_2.

1. Introduction

Tetrahydrofurfuryl alcohol (THFA) is an essential precursor and environmentally friendly solvent in high demand in printer inks, and agricultural and automotive industries.[1–4] In industry, Cu–Cr and noble metal catalysts are used to catalyze the two-step conversion of furfural (FFR) to THFA, where the first step converts FFR to furfuryl alcohol (FFA) and the second step transforms FFA into THFA,[5–7] which is an environmentally unfriendly and complex process with high energy consumption and yielding many undesirable products, such as 2-methylfuran (2-MF), 2-methyltetrahydrofuran (2-MTHF), cyclopentanone (CPO) and cyclopentanol (CPA), furan, and tetrahydrofuran[8,9] (Scheme 1a). Recently, researchers have focused on developing highly efficient catalysts for the one-step conversion of FFR into THFA, which is more economic and convenient.[10–12] Although significant progress has been achieved, selective hydrogenation of FFR still faces challenges since many undesired products can be created owing to the high temperatures and high hydrogen pressures.[13–16] Also, the harsh reaction conditions in THFA production may cause extra infrastructural costs to a large degree. Although noble metal-based catalysts, such as Pd and Ru, can efficiently catalyze the synthesis of THFA from FFR, the high cost and scarce reserves have prompted a desperate search to find efficient non-precious metal catalysts.[17–19] Especially, Ni-based catalysts have garnered significant attention in the field of hydrogenation reactions due to their cost-effectiveness and high activation capacity for hydrogen.[20,21] However, the easy deactivation at high temperatures, the weak affinity between metal nanoparticles and FFR molecules, and the poor reusability of Ni-based catalysts render them unfavorable for high-efficiency hydrogenation reactions under mild conditions. Therefore, the rational design and preparation of non-noble metal catalysts, especially Ni-based catalysts, for FFR hydrogenation to achieve satisfactory selectivity toward THFA under mild conditions, remains a great challenge.

Metal–organic frameworks (MOFs),[22] assembled by inorganic metal ions/clusters and organic linkers, have been widely used in various fields, such as gas storage and separation,[23–26] and catalysis.[27–30] Due to the large surface area, adjustable pore size, and the potential for surface functionalization, MOFs have proven to be excellent templates for converting into various

[a] School of Materials Science and Engineering, Qilu University of Technology (Shandong Academy of Sciences), Jinan 250353, P. R. China. E-mail: zhaoxuebo@upc.edu.cn
[b] College of Chemistry and Chemical Engineering, China University of Petroleum (East China), Qingdao, 266580, P. R. China
[c] School of Science and Engineering, The Chinese University of Hong Kong, Shenzhen 518172, P. R. China. E-mail: yanglingzhi@cuhk.edu.cn
[d] School of Petrochemical Engineering, Liaoning Petrochemical University, Liaoning 113001, P. R. China. E-mail: fswhy@126.com

† Electronic supplementary information (ESI) available. See DOI: https://doi.org/10.1039/d3ma00938f

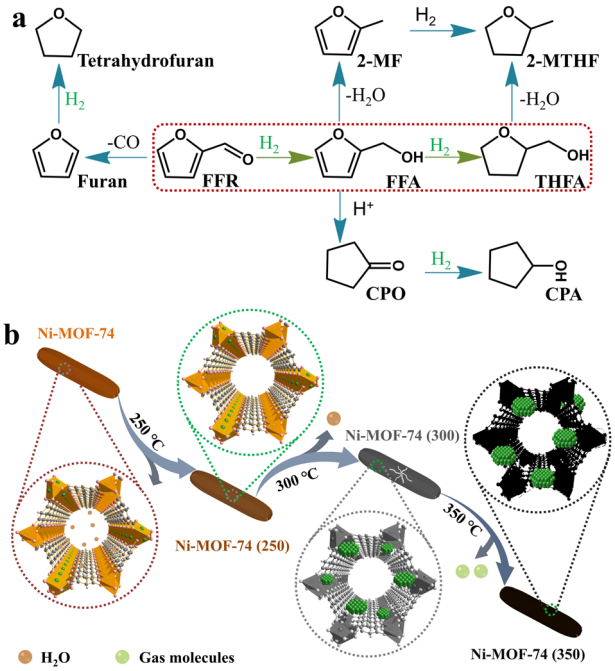

Scheme 1 (a) Reaction pathways and byproducts for the conversion of FFR to THFA, and (b) schematic illustration for the structural changes of the Ni-MOF-74.

porous carbon/metal-based nanomaterials while preserving the merit of pristine MOFs to some extent.[31–35] Generally, a template strategy combining metal nanoparticles with MOFs has been considered to achieve enhanced performance, especially in catalysis.[36] Several strategies have been testified to integrate metal nanoparticles and MOFs, and among them, thermal decomposition is relatively normal and facile to realize.[37–40] However, harsh heat treatment conditions usually cause the MOF framework to collapse and lose intrinsic porosity, which somewhat hinders the exposure of partially active sites.[41,42] Recently, Quasi-MOFs, which possess the advantages of both exposed inorganic nodes and preserved porosity, have been reported by partially decomposing MOFs.[43,44] The strong metal–support interactions that existed in Quasi-MOFs can significantly enhance the catalytic performance, and the porous structure partially retained is conducive to accelerating the diffusion of substrates. Xu *et al.* first reported Quasi-MOF structures with both porous structures and strong interactions between Au particles and inorganic Cr–O nodes by controlled deligandation, which exhibited improved catalytic performance in CO oxidation at low temperatures.[45] Shen *et al.* synthesized a novel Cu-nanowire@quasi-MOF *via* partial thermal decomposition, and the catalyst exhibited excellent catalytic performance for the selective oxidation of benzyl alcohol in the air.[46] However, the introduction of additional metal ions complicates the synthesis process and obscures the interactions between the metal and inorganic nodes. Besides, external metals may cause blockage of the channels and impede the active site accessibility of the reactants.[47] Therefore, the construction of Quasi-MOFs with special pores and abundant metal active sites is exceptionally important for catalytic reactions.

Starting from the extraordinary properties of Quasi-MOF and combining with the high activity features of Ni-based catalysts, herein, Quasi-MOFs with unique hub-and-spoke channels and abundant Ni nanoparticles were prepared for the total hydrogenation of FFR. Homogeneous Ni nanoparticles encapsulated in Quasi-MOFs were obtained *via* partial deligandation of Ni-MOF-74. The Ni-MOF-74 framework provided Ni sources and supports stabilizing the Ni nanoparticles. Besides, the surface NiO species were generated during the deligandation process, which facilitates the adsorption of FFR/H_2 molecules. The optimized Quasi-MOF-9h sample exhibited significantly boosted catalytic activity and stability. It only needed a moderate temperature to achieve a 98% yield of THFA in ethanol, ranking it the best among the reported Ni-based catalysts. The unique spokewise pore channels, abundant Ni^0, and surface NiO species in the Quasi-MOF-9h sample ultimately contributed to the high catalytic performance of the total hydrogenation reaction.

2. Experimental

2.1. Synthesis of Ni-MOF-74 products

According to the previous work, 0.78 g of 2,5-dihydroxyterephthalic acid ($C_8H_6O_6$), 1.99 g of nickel acetate tetrahydrate ($Ni(OAc)_2{\cdot}4H_2O$), and 50 mL of deionized water were put in a Teflon lined stainless steel autoclave.[48] Subsequently, the autoclave was sealed and transferred to an oven at 160 °C for 5 h. After cooling to room temperature, the resulting dark yellow solid product was collected by centrifugation, washed three times with water, and dried at 80 °C overnight. The obtained sample was labelled as Ni-MOF-74.

2.2. Synthesis of Ni-MOF-74 (*T*) samples

To prepare Ni-MOF-74 (*T*) samples, the obtained Ni-MOF-74 was placed in a tube furnace and heat-treated at a specific temperature (the heating rate was maintained at 5 °C min^{-1}) under an argon atmosphere (50 mL min^{-1}). The products were denoted as Ni-MOF-74 (*T*), where *T* represents the heat treatment temperature.

2.3. Synthesis of Quasi-MOF catalysts

Ni-MOF-74 was placed in a tube furnace and decomposed at 300 °C (the heating rate was maintained at 5 °C min^{-1}) under an argon atmosphere. In this process, heat treatment was carried out for different periods, and the argon flow rate was maintained at 50 mL min^{-1}. The products were denoted as Quasi-MOF-*X*, where *X* represents the pyrolysis time (*X* = 3 h, 6 h, and 9 h). Especially, the sample treated for 12 h was named Ni/NiO/C-12h.

2.4. Material characterization

X-ray diffraction (XRD) patterns were collected on a PANalytical X'Pert PRO MPD X-ray diffractometer using Cu Kα radiation. Transmission electron microscopy (TEM) was performed using a JEM-2100UHR instrument (JEOL) at 200 kV. The morphological properties of products were studied by using a Hitachi S-

4800 field-emission scanning electron microscope (SEM). The Raman spectrum was recorded using a Horiba Scientific LabRAM HR Evolution, with a laser excitation wavelength of 633 nm. Thermogravimetric (TG) analysis data were obtained on a TG209F3 (NETZSCH) thermogravimetric analyzer with a heating rate of 10 °C min^{-1} under a N_2 atmosphere. Gases generated from the heat-treatment process of Ni-MOF-7 were measured by mass spectrometry (MS) (Hiden HPR-20). The textural properties of samples were obtained using nitrogen physical adsorption isotherms at 77 K on Quantachrome Autosorb-iQ nitrogen volumetric adsorption apparatus. Before measurement, the MOF-74 and carbonized samples were activated for 12 h under vacuum at 150 °C and 200 °C, respectively. X-ray photoelectron spectra (XPS) were obtained using an X-ray photoelectron spectrometer (ESCALAB 250Xi) equipped with monochromatic Al Kα (E = 1486.6 eV) radiation. The measured XPS energies were collected using the C 1s peak of the C–C bond at 284.8 eV. An inductively coupled plasma-optical emission spectrometer (ICP-OES, Agilent 720ES) was used to determine the Ni elemental content.

The hydrogen adsorption capacity of the catalysts was measured using hydrogen temperature-programmed desorption (H_2-TPD), which was conducted with a Builder PCA-1200 TPD/TPR instrument equipped with a thermal conductivity detector (TCD). In the program of H_2-TPD, the sample (50 mg) was sealed in a quartz tube, followed by activating at 250 °C for 1 h under H_2/Ar gas to remove solvents trapped in the channels and to reduce the oxidized sample surface before hydrogen adsorption. Then, under H_2/Ar protection, the sample was cooled to 60 °C. Subsequently, the sample was exposed to H_2/Ar (1 : 9, v/v, 30 mL min^{-1}) for 1 h to ensure that the metal sites were saturated with hydrogen. Next, the sample was slowly purged with Ar (30 mL min^{-1}) to remove the adsorbed physical H_2 on the sample surface. After the baseline was stabilized, the sample was heated to 300 °C at a rate of 10 °C min^{-1}. In this process, the desorption signal of H_2 was detected by TCD.

2.5. Catalytic evaluation

The selective hydrogenation of FFR was carried out in a stainless autoclave (Beijing Century Senlong, SML-100) with a mechanical stirrer and a temperature controller unit. In a typical experiment, 0.6 g of FFR, 50 mL of ethanol, and 0.1 g of catalyst were added to the reactor. After the reactor was sealed, the reaction system was purged with H_2 three times to exclude air and then filled with the initial hydrogen H_2 pressure to a setting value. The reaction was held at a specific temperature (50–90 °C), and the stirring speed was set at 800 rpm. After the reaction, the autoclave was cooled down quickly, and the catalysts were collected by centrifugation and washed three times with ethanol.

2.6. Analysis of products

The liquid products were analyzed on a chromatograph equipped with a capillary column and a flame ionization detector (FID). The temperature of the sample injector and detector were set as 200 °C and 250 °C, respectively. The products were identified by comparing them with authentic samples, and the reactants and products were quantified by the normalization method. The conversion of FFR (C_{FFR}) and the selectivity of THFA (Y_{THFA}), FFA (Y_{FFA}), and byproducts ($Y_{byproducts}$) are calculated using the formulae as follows.

$$C_{FFR} = \frac{n_{FFR,0} - n_{FFR,t}}{n_{FFR,0}} \times 100 \quad (1)$$

$$Y_{FFA} = \frac{n_{FFA,t}}{n_{FFR,0} - n_{FFR,t}} \times 100\% \quad (2)$$

$$Y_{THFA} = \frac{n_{THFA,t}}{n_{FFR,0} - n_{FFR,t}} \times 100\% \quad (3)$$

$$Y_{byproducts} = 1 - Y_{FFA} - Y_{THFA} \quad (4)$$

In which $n_{FFR,0}$ represents the initial mole of FFR before the reaction, $n_{FFR,t}$ is the mole of FFR in the reaction, $n_{FFA,t}$ is the mole of FFA during the reaction, and $n_{THFA,t}$ is the mole of THFA during the reaction.

3. Results and discussion

3.1. Characterization of catalysts

The XRD patterns of the as-prepared Ni-MOF-74 and Ni-MOF-74 (T) samples are shown in Fig. 1a. According to the XRD pattern of the synthesized Ni-MOF-74, two prominent sharp signature diffraction peaks located at 2θ values of 6.9° and 11.9° match well with the simulated pattern, indicating the successful preparation of the precursor. The Ni-MOF-74 (250) sample displayed the same pattern as Ni-MOF-74, implying the integrity of the framework structure at this treated temperature. It is noteworthy that three weak characteristic peaks positioned at 44.5°, 51.8°, and 76.3° appeared in the Ni-MOF-74 (300) sample, which corresponds to the (111), (200) and (220) lattice planes of the standard face-centered cubic (fcc) Ni phase (JCPDS card no. 04-0850), respectively. The dominant phase presented in the Ni-MOF-74 (300) sample is still the characteristic peaks of Ni-MOF-74. This demonstrates that after treatment at 300 °C, partial ligands begin to decompose, and the aggregated Ni clusters are converted into metallic Ni nanoparticles *in situ*. Moreover, the broad Ni peaks indicate the small particle size of Ni metal nanoparticles, which could endow the sample with high catalytic activity.[49] When the temperature reaches 350 °C, the characteristic peaks attributed to Ni-MOF-74 disappear entirely, demonstrating the complete collapse of the Ni-MOF-74 framework. In the meantime, the enhanced intensity of Ni peaks indicates a larger particle size in the Ni-MOF-74 (350) sample. Thermogravimetric (TG) analysis was performed to monitor the thermal behavior of Ni-MOF-74 (Fig. S1, ESI†). The TG result shows that the Ni-MOF-74 structure begins to collapse above 300 °C, consistent with the structure evolution in XRD results.

The specific surface area and pore structure characteristics of the Ni-MOF-74 precursor and Ni-MOF-74 (T) samples were investigated *via* N_2 physisorption tests. As displayed in Fig. 1b,

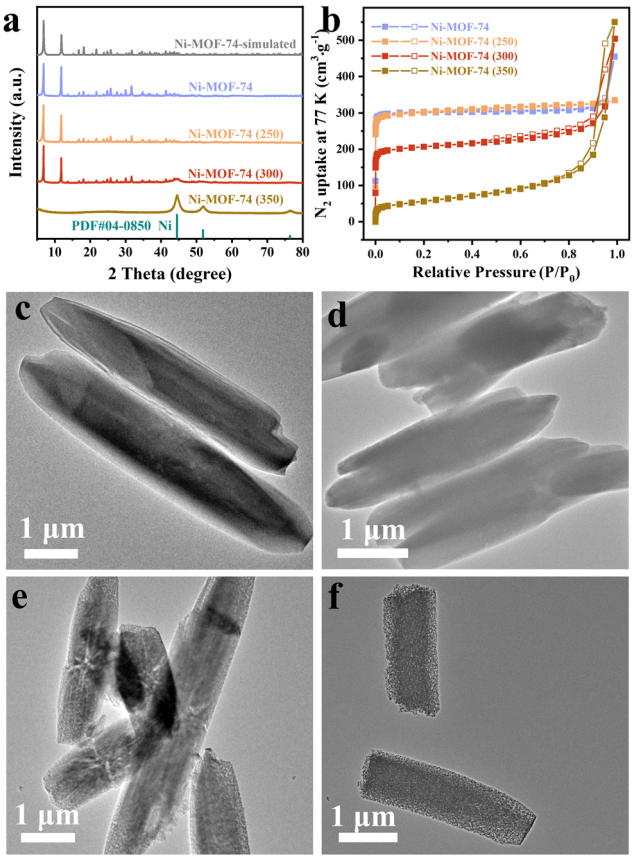

Fig. 1 (a) XRD patterns of the Ni-MOF-74 precursor and Ni-MOF-74 (*T*) samples, (b) N_2 adsorption–desorption isotherms at 77 K of the Ni-MOF-74 precursor and Ni-MOF-74 (*T*) samples. TEM images of (c) Ni-MOF-74 precursor, (d) Ni-MOF-74 (250), (e) Ni-MOF-74 (300) and (f) Ni-MOF-74 (350).

the Ni-MOF-74 precursor and Ni-MOF-74 (250) sample all exhibit type I isotherms based on the IUPAC classification, which indicates the existence of abundant micropores. The specific surface area of the Ni-MOF-74 (250) is measured to be 1238 $m^2\ g^{-1}$ (Table S1, ESI†), almost entirely the same as the precursor (1255 $m^2\ g^{-1}$), further implying the integrity of the Ni-MOF-74 (250) sample framework. The Ni-MOF-74 (300) sample shows a typical type I/IV isotherm with a sharp rise near $P/P_0 = 0$ and a hysteresis loop at $0.5 < P/P_0 < 0.99$, indicating the presence of both microporous and mesoporous structures. The specific area of the Ni-MOF-74 (300) could be retained by 66% (823 $m^2\ g^{-1}$), and the mesopore distribution is concentrated in the range of 25–35 nm (Fig. S2, ESI†), confirming the partial collapse of the framework. With a further increase in the pyrolysis temperature, the surface area of the Ni-MOF-74 (350) only retained 15.7% (197 $m^2\ g^{-1}$), with a pore size focused on 15–20 nm (Fig. S2, ESI†). The smaller pore size in Ni-MOF-74 (350) indicates that the sample is incapable of generating unique spokewise channels at this heat treatment temperature, which will be evidenced later in the TEM images. The disappearance of micropores illustrates the complete collapse of the Ni-MOF-74 framework, as confirmed by the XRD results. Therefore, the Ni-MOF-74 (300) sample possesses a unique hierarchical porous structure, which is favorable for the maximum exposure of the active catalytic sites and the shuttling of the substrate molecules.

The morphology and structure of the prepared Ni-MOF-74 and Ni-MOF-74 (*T*) samples were investigated by transmission electron microscopy (TEM). It is obvious that the Ni-MOF-74 crystals are smooth and uniform hexagonal rod-shaped with an average diameter of about 1 μm, and the heat-treated samples perfectly inherit the morphology of the precursors (Fig. 1c–f and Fig. S3 and S4, ESI†). Meanwhile, the structure of the Ni-MOF-74 (250) sample was well maintained (Fig. 1d and Fig. S5, ESI†) since the decomposition of the Ni-MOF-74 framework could not occur at this temperature. Interestingly, remarkable hub-and-spoke channels can be seen in the inside of the Ni-MOF-74 (300) nanorods (Fig. 1e). Besides, the width of the spokewise channels was measured and found to be approximately 30 nm (Fig. S6, ESI†), consistent with the mesopore size distribution discussed above. As the annealing temperature reaches 350 °C, the metal particles are uniformly distributed, and no spokewise phenomenon is observed (Fig. 1f). Also, larger metal Ni nanoparticles are observed in the Ni-MOF-74 (350) sample, which agrees well with the XRD results. This phenomenon suggests that the presence of hub-and-spoke channels is highly dependent on the heat treatment temperature. It has been conjectured that the specific temperature induces a slight contraction beginning at the external surface of the sample, accompanied by abundant gas escaping from the internal region of the sample, hence leaving this unique hub-and-spoke channel. Mass spectrometry (MS) results have confirmed the steady and consistent escape of gas at this temperature (Fig. S7, ESI†).

Based on the results above, the structural evolution of Ni-MOF-74 is illustrated in Scheme 1b. When treated at 250 °C, the Ni-MOF-74 weight loss could be attributed to the removal of coordinated guest molecules (H_2O) inside the channels. Further raising the pyrolysis temperature to 300 °C, the deligandation process begins to occur by releasing a certain amount of gases, such as H_2 and CO, and obtaining Ni^0 (as confirmed by XRD results),[50] obtaining a Quasi-MOF structure (Thus, the Ni-MOF-74 (300) sample is renamed Quasi-MOF-3h hereafter). As the pyrolysis temperature was higher than 300 °C, the framework collapsed due to the complete decomposition of the organic linkers. In addition, the uniform and rapid decomposition of ligands at 350 °C did not leave spokewise channels as in the Quasi-MOF-3h sample. To better understand the evolution process of the Quasi-MOF structure, the investigation was carried out by extending the heat treatment time of Ni-MOF-74 at 300 °C.

On prolonging the pyrolysis time from 3 h to 9 h, the characteristic diffraction peaks around 5°–15° in Ni-MOF-74 decreased, indicating a consistent deligandation of Ni-MOF-74 (Fig. 2a). This unique structure containing both partial frameworks of the MOF and Ni metal particles is denominated as the Quasi-MOF for convenience of description. Interestingly, Ni nanoparticles exhibit remarkable tolerance against aggregation in the deligandation process, implying that a strong interaction

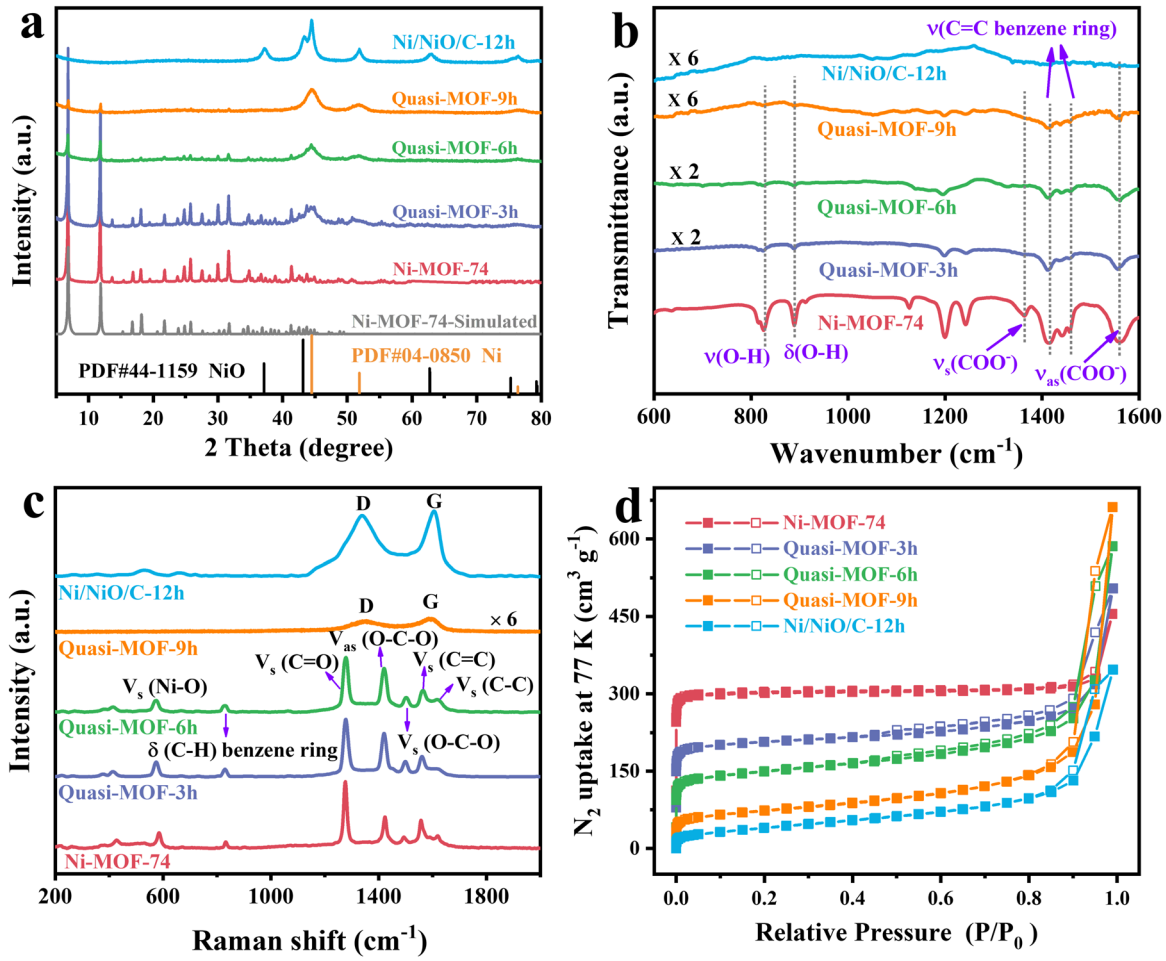

Fig. 2 (a) XRD patterns, (b) FT-IR spectra, (c) Raman spectra and (d) N_2 adsorption–desorption isotherms for the Ni-MOF-74 precursor and the derivatives.

exists between inorganic nodes Ni–O and metallic Ni nanoparticles in the Quasi-MOF.[7,45] Upon further extension of the heat treatment time to 12 h, the disappearance of the diffraction peaks of Ni-MOF-74 implies complete decomposition of the ligand. The diffraction peaks of trigonal NiO (JCPDS no. 44-1159) appeared at 2θ = 37.2°, 43.3°, 62.9° and 75.4°, which can be ascribed to the (101), (012), (110) and (113) crystal planes of NiO, respectively. The intensity of metal Ni peaks increases and the peak width decreases obviously in the Ni/NiO/C-12h sample, indicating that the disappearance of the Quasi-MOF framework leads to the aggrandizement of the Ni particles. Besides, owing to the particular lower heat treatment temperature, the metallic Ni was gradually oxidized to NiO prolonging the heat treatment time, which will be discussed in detail later.

The structure evolution of Quasi-MOF was further investigated by FT-IR spectroscopy (Fig. 2b). The absorption bands centered at 1361 and 1557 cm^{-1} of the Ni-MOF-74 sample are attributed to the symmetric and asymmetric vibration modes of $-COO^-$ coordinated to the Ni ions, proving the existence of the coordination reaction between Ni ions and –COOH groups in the ligands.[51] The vibration peaks at 824 and 888 cm^{-1} in the Ni-MOF-74 sample are assigned to the C–H bending of the benzene ring.[50] The peaks located at 1414 and 1457 cm^{-1} could be attributed to the C=C stretching vibration modes, which belong to the benzene ring skeleton vibration.[50,52] The intensity of the characteristic peaks gradually decreased with the extension of the heat treatment time, indicating that a slow deligandation process of Ni-MOF-74 occurred. Therefore, the existence of the MOF framework was further demonstrated by the characteristic peaks in the samples, indicating the Quasi-MOF properties. When the annealing time was increased to 12 h, all the peaks mentioned above belonging to Ni-MOF-74 vanished, validating the collapse of the Ni-MOF-74 framework. Raman spectroscopy was performed to get insight into the structural evolution of the samples during the deligandation process. The Raman spectra of Quasi-MOF-3h and Quasi-MOF-6h are almost identical to that of Ni-MOF-74 (Fig. 2c), except for the decreased peak intensity and the broadened peaks, again confirming the occurrence of the deligandation of Ni-MOF-74. However, when the heat treatment time was extended to 9 h, the peaks belonging to Ni-MOF-74 disappeared, and two weak peaks belonging to disordered carbon (D band) and graphitic carbon (G band) occurred. The disappearance of MOF-74 peaks in the Quasi-MOF-9h sample might be attributed to the

presence of the carbon layer masking the weaker MOF characteristic peaks, which is inconsistent with the XRD and FT-IR tests. For Ni/NiO/C-12h, two strong broad peaks were observed, indicating the complete decomposition of Ni-MOF-74 with carbon formation. This phenomenon indicates that the transformation of Ni-MOF-74 to Ni/NiO/C-12h is a sluggish deligandation process *via* the Quasi-MOF intermediate. No carbon peaks could be observed due to the slow decomposition of ligands until the heat treatment time is extended to 9 h. Furthermore, the intensity of carbon peaks increases obviously with further prolonging the heat treatment time. The occurrence of the thinnish carbon layer helps to improve the stability of the sample and prevents Ni particles from aggregating, achieving good catalytic performance,[53] while the thicker carbon layer obstructs the contact between the reactants and active sites, leading to poor catalytic activity.

The N_2 adsorption–desorption isotherms of the derivatives all display typical type I/IV isotherms (Fig. 2d). On extending the heat treatment time, the ligands in Ni-MOF-74 gradually decomposed. The surface areas of the Quasi-MOF-6h and Quasi-MOF-9h samples regularly decreased to 563 $m^2\ g^{-1}$ and 261 $m^2\ g^{-1}$, respectively (Table S2, ESI†). Furthermore, it was found that the Quasi-MOF-9h sample has the highest contents of mesopores concentrated at 25–35 nm, indicating that it has the most abundant hub-and-spoke channels (Fig. S8, ESI†). The percentage of micropores regularly decreases from 87.48% (Quasi-MOF-3h) to 32.57% (Quasi-MOF-9h) as the heat treatment time increases (Fig. S9 and S10, ESI†), while the total pore volume displays an opposite trend (Table S2, ESI†). The highest value of a total pore volume of 1.02 $cm^3\ g^{-1}$ was formed in the Quasi-MOF-9h sample, and then decreased to 0.54 $cm^3\ g^{-1}$ by increasing the heat treatment time to 12 h. The high porosity not only dramatically improves the mass transfer capacity of the reactants, but also facilitates the dispersion and exposure of active sites on the catalyst, hence improving the accessibility of the active sites.

The morphology and the structure of metal particles of derivatives were observed by SEM images, and the results are given in Fig. 3. It is obvious that all Ni-MOF-74 derivatives maintained the hexagonal rod-like morphology of the precursor well. As shown in Fig. $3a_1$, many pores and cracks can be seen on the surface of the Quasi-MOF-3h sample due to gas escape. After 6 h of heat treatment, the surfaces of the Ni-MOF-74 hexagonal rod become rough and the reduced metal Ni nanoparticles are observed clearly (Fig. $3b_1$), indicating that further decomposition of the framework led to a higher reduction degree of metallic Ni nanoparticles. Fig. $3c_1$ depicts a further increase in the surface roughness of the sample and even slight agglomeration due to the improvement in the reduction degree of the Quasi-MOF-9h sample. As shown in Fig. $3d_1$, the Ni/NiO/C-12h sample is composed of metal nanoparticles with uniform particle sizes. Mesoporous pores and cracks are evident on the sample surface (Fig. S11, ESI†). To sum up, Quasi-MOF samples, which possessed both confined Ni nanoparticles and preserved partial framework of the Ni-MOF-74, can be successfully obtained by controlling partial deligandation at 300 °C.

The surface microstructure features of the Ni-MOF-74 derivatives were probed by TEM measurements. Notably, the unique hub-and-spoke channels generated by gas escape and framework shrinkage are found in all derivatives (Fig. $3a_2$–d_2), confirming the importance of the pyrolysis temperature in this unique channel structure. The enlarged TEM images (Fig. $3a_3$–d_3) of Quasi-MOF samples demonstrate that these Ni nanoparticles are uniformly dispersed, ensuring adequate exposure of active catalytic sites. From the size distribution of metallic Ni particles, the average size of metallic Ni nanoparticles in the Quasi-MOF-3h, Quasi-MOF-6h, Quasi-MOF-9h and Ni/NiO/C-12h samples corresponds to 3.9 nm, 4.2 nm, 4.8 nm, and 6.5 nm, respectively (illustration in Fig. $3a_3$–d_3), suggesting that the heat treatment time has a great influence on the size of metal particles. HRTEM tests were conducted to probe structure changes around Ni nanoparticles in Quasi-MOF samples. In the Quasi-MOF-3h and Quasi-MOF-6h samples, a softer color of metallic Ni can be found in HRTEM images, and there is no carbon layer around metallic Ni nanoparticles, confirming the relatively low reduction degree and the occurrence of the deligandation process (illustration in Fig. $3a_3$ and b_3). For the Quasi-MOF-9h sample, the particle size of Ni nanoparticles marginally increases with 1–2 layers of amorphous carbon formed around the particles (Fig. S12, ESI†), which is consistent with Raman results. The *d*-spacing of 0.203 nm assigned to the (111) crystal plane of metal Ni and 0.241 nm owing to the (101) crystal plane of NiO can be observed in the Ni/NiO/C-12h sample (Fig. S13, ESI†), confirming the presence of NiO. Besides, 3–4 layers of amorphous carbon and strong D and G bands can be found in the Ni/NiO/C-12h sample, indicating a high degree of carbonization.

Therefore, Ni-MOF-74 undergoes a sluggish deligandation process by prolonging the heat treatment time at 300 °C. The organic ligands gradually decompose to release CO, H_2 and other gases, while partial adjacent Ni atoms migrate together to form Ni metal particles under the protection of a reducing gas, obtaining the Quasi-MOF structure with unique hub-and-spoke channels. During the deligandation process, the remaining robust MOF-74 framework further prevents Ni metal particles from agglomeration. When the heat treatment time was increased to 12 h at 300 °C, the Quasi-MOF structure vanished, although the unique hub-and-spoke channels existed. In contrast, the Quasi-MOF structure and distinctive spokewise channels were unavailable when the heat treatment temperature was increased to 350 °C, revealing that both the heat treatment temperature and time were critical to acquiring the specialized structure.

To further get insight into the effects of heat treatment conditions on the elemental composition and atomic valence state in Ni-MOF-74 derivatives, X-ray photoelectron spectroscopy (XPS) was carried out. Quasi-MOFs and Ni/NiO/C-12h contain C, O and Ni elements according to the full XPS spectra (Fig. S14, ESI†). C 1s can be divided into three peaks at 284.8 eV, 285.8 eV and 288.8 eV, belonging to C═C, C–O and O═C–O, respectively (Fig. S15, ESI†).[41] For Ni $2p_{3/2}$ spectra in Quasi-MOFs, three peaks appear at binding energies of 853 eV,

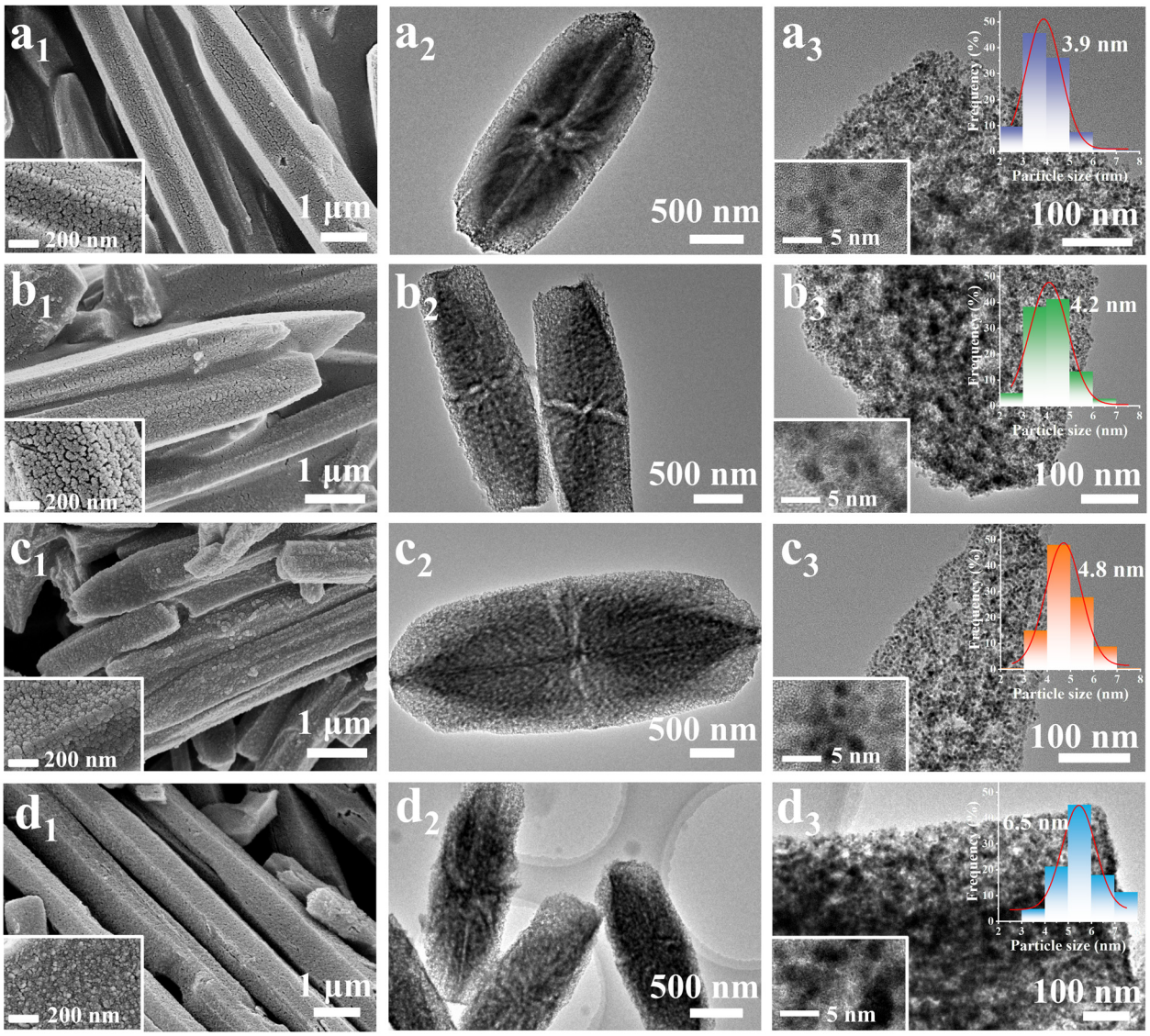

Fig. 3 Electron microscopy images of (a) Quasi-MOF-3h, (b) Quasi-MOF-6h, (c) Quasi-MOF-9h, and (d) Ni/NiO/C-12h samples. Column 1: SEM images and the corresponding local magnification; Column 2: TEM images; and Column 3: TEM, HRTEM, and particle size distribution profile.

856.2 eV and 861.4 eV, assigned to Ni^0, Ni^{2+} and their accompanying peak, respectively (Fig. 4a).[54] It is distinct from the structural integrity of the Ni-MOF-74 (250) sample containing only Ni^{2+} species (Fig. S16, ESI†). Interestingly, a new peak with a binding energy centered at 854.1 eV (denoted as $Ni^{2+,surf}$) observed, assigned to the surface NiO species as Palacín reported.[55] NiO is composed of surface Ni atoms (NiO_5 in pyramidal) with deficiency and bulk Ni atoms (NiO_6 in octahedral), therefore, showing a multi-peak structure in the XPS spectrum.[55] The presence of $Ni^{2+,surf}$ implies the formation of abundant highly-dispersed NiO nanoclusters during the decomposition process of the Quasi-MOF.[56] It is deduced that the newly formed surface NiO species are electronically defective, which modulates the electronic structure of metallic Ni. The Ni 2p spectrum suggests that the content of surface NiO species increases with prolonging the heat treatment time. Therefore, we inferred that Ni atoms are gradually *in situ* reduced to ultrathin Ni metal particles during the slow deligandation process of Ni-MOF-74 at 300 °C. The large surface energy of the ultra-small Ni particles drove the O atoms in the ligand to bind to them, generating NiO nanoclusters (surface NiO species) attached to the Ni particle surface. However, the NiO nanoclusters were too tiny to be detected by XRD instruments. The content of NiO nanoclusters increased gradually with the extension of the heat treatment time, and the NiO nanoclusters aggregated into large particles that can be easily recognized when treated with 12 h. For convenient understanding, Ni^{2+} peaks were divided into surface NiO species (red color), bulk NiO peaks (green color) and Ni^{2+} in the MOF framework (blue color) (Fig. 4a). Besides, the O 1s spectrum also confirms the change in the content of the Ni–O bond, corresponding to an increase of surface NiO species in the

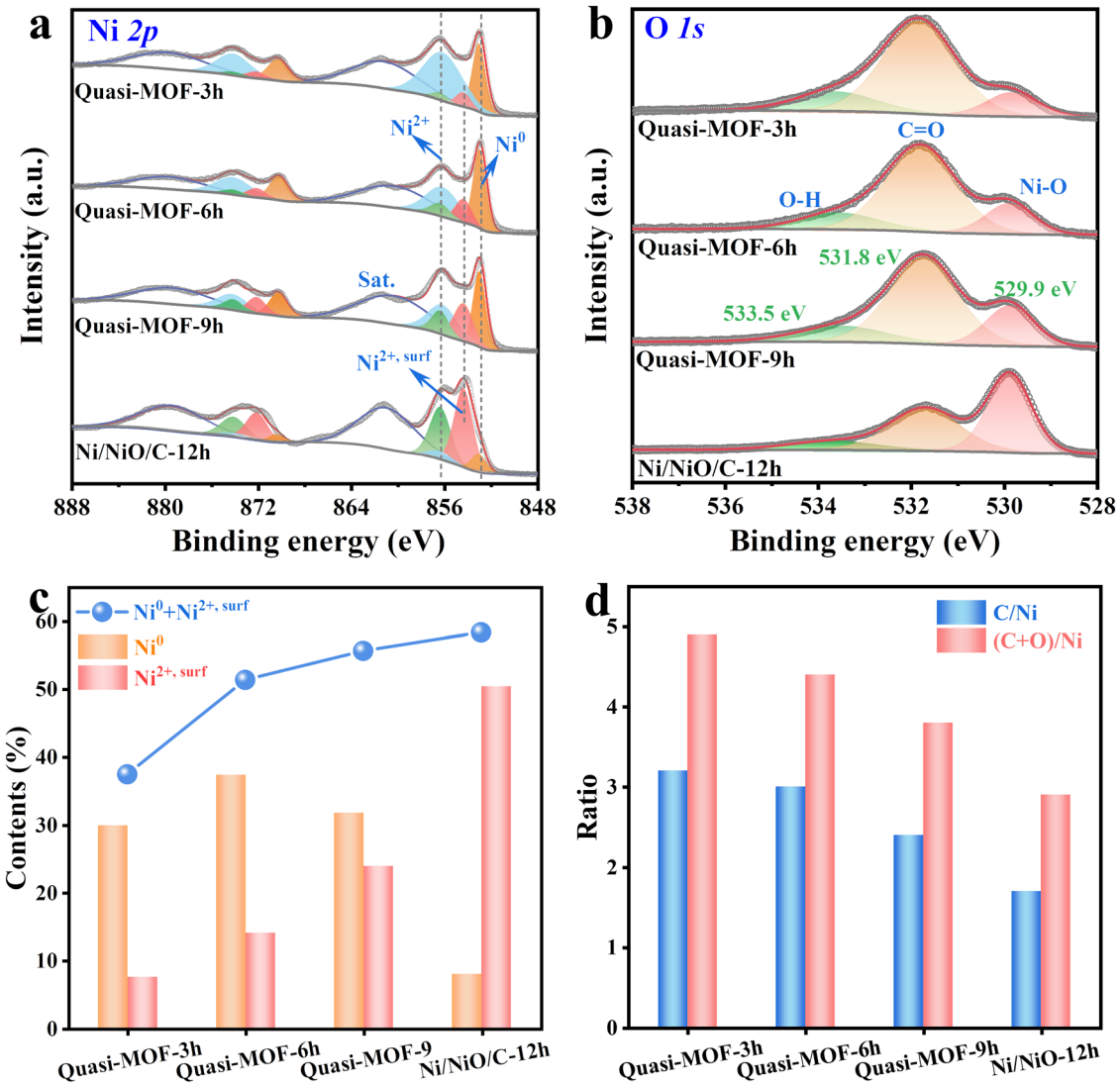

Fig. 4 The high-resolution XPS of Quasi-MOF-3h, Quasi-MOF-6h, Quasi-MOF-9h and Ni/NiO/C-12h: (a) Ni 2p spectra (note: orange color represents for Ni^0, red color represents for $Ni^{2+,surf}$, green color represents for Ni^{2+} in NiO, and the blue color represents for Ni^{2+} in Ni-MOF-74) and (b) O 1s spectra. (c) Changes in the elemental area ratios of Ni^0, $Ni^{2+,surf}$, and Ni^0 + $Ni^{2+,surf}$. (d) Elemental atomic ratio of C, and C + O relative to Ni.

Quasi-MOFs samples (Fig. 4b). The elemental contents of Ni and (Ni^0 + $Ni^{2+,surf}$) increased upon extending the heat treatment time, which indicates an increase in the deligandation degree of Ni-MOF-74 precursors (Fig. 4c and Table S3 and S4, ESI†). Besides, ICP-OES also confirmed the increasing trend of the Ni content (Table S5, ESI†). As shown in Fig. 4d, the value of both C/Ni and (C + O)/Ni in derivatives all display a decreasing trend upon prolonging the heat treatment time. The decreased amount of C and O elements indicates that the ligands are gradually decomposed during the deligandation process. Only a tiny amount of Ni^0 is visible in the Ni/NiO/C-12h sample owing to the extended heat treatment, consistent with the XRD results (Fig. 4a and Fig. S17 and 18, ESI†). This unique surface $Ni^{2+,surf}$ species, which can only be obtained in Quasi-MOF structures, is found neither in Ni-MOF-74 (250) with a complete MOF framework nor in Ni-MOF-74 (350) possessing a complete collapsed framework (Fig. S19, ESI†). The above results indicated that the heat treatment temperature and time could significantly affect the elemental composition and atomic valence state. High temperatures facilitate the sluggish reduction of highly dispersed oxide nanoclusters by carbon, while extended heat treatment time at low temperatures gives rise to slow oxidation of metals. Therefore, it is vital to precisely control the reaction conditions to obtain the Quasi-MOF with abundant Ni^0, surface $Ni^{2+,surf}$ species and unique hub-and-spoke channels.

3.2. Catalytic test

To investigate the catalytic performance of the prepared Quasi-MOF samples, the hydrogenation of FFR to THFA was carried out under liquid-phase conditions. The results showed that the hydrogenation reaction could not occur without a catalyst (Table 1, entry 1). Without catalysts, all the products achieved were 2-(diethoxymethyl)furans (2-DEMF), obtained by the

Table 1 The catalytic performance of derivatives of Ni-MOF-74

Entry	Catalysts	Conversion (%)	Selectivity (%)		
			FFA	THFA	2-DEMF
1	none	3.2	0	0	100
2	Ni-MOF-74	5	0	0	100
3	Ni-MOF-74 (250)	5.7	0.8	0	99.2
4	Ni-MOF-74 (300) (Quasi-MOF-3h)	91.4	70.3	29.6	0.1
5	Ni-MOF-74 (350)	91.4	80	19.9	0.1
6	Quasi-MOF-6h	>99	29.2	70.7	0.1
7	Quasi-MOF-9h	>99	13.2	86.7	0.1
8	Ni/NiO/C-12h	68.1	73.8	26.1	0.1

Reaction conditions: 0.6 g of FFR, 0.1 g of catalysts, 50 mL of ethanol, 60 °C, 3 MPa, 4 h.

condensation reaction of FFR and ethanol (Fig. S20, ESI†).[47] In addition, Ni-MOF-74 and Ni-MOF-74 (250) were catalytically inactive for the THFA formation due to the absence of active sites of metallic Ni in the samples (Table 1, entries 2 and 3). The Ni-MOF-74 (300) catalyst displayed dramatically improved catalytic performance, with 91.4% conversion of FFR and 29.6% selectivity to THFA after 4 h of reaction (Table 1, entry 4), which could be ascribed to the existence of special hub-and-spoke channels as well as the presence of both metallic Ni and surface $Ni^{2+,surf}$ species. On the one hand, adequate metallic Ni, as well as $Ni^{2+,surf}$ species, can be functioned to tightly adsorb FFR/H_2. On the other hand, abundant hub-and-spoke channels endow Ni-MOF-74 (300) with excellent mass transfer capability and more exposed catalytic active sites, allowing improved contact between the reactants and active sites. The selectivity to THFA was decreased to 19.9% when choosing the Ni-MOF-74 (350) sample as the catalyst (Table 1, entry 5). Although the Ni clusters in precursors were transformed into metallic Ni in the Ni-MOF-74 (350) catalyst, the absence of the unique hub-and-spoke channel and the expansion of the metal nanoparticles lowered the hydrogenation catalytic activity (Fig. S21, ESI†).

Next, the hydrogenation performance of the Quasi-MOF samples and Ni/NiO/C-12h was investigated under the same conditions. Using the Quasi-MOF-6h sample as the catalyst, the conversion of FFR was higher than 99% and the selectivity of THFA was remarkably increased to 70.7%, which could be ascribed to the corresponding increase in the number of active sites (Table 1, entry 6). When the Quasi-MOF-9h sample was chosen as the catalyst, excellent catalytic activity was achieved, with the complete transformation of FFR and 86.7% selectivity to THFA (Table 1, entry 7). Further extension of the heat treatment time to 12 h resulted in a sharp decrease in the hydrogenation activity, the FFR conversion dropped to 68.1%, and the selectivity of THFA was only 26.1% (Table 1, entry 8). Considering that there is no obvious difference in the particle size in the Quasi-MOF, the variation in catalytic performance is attributed to the differences in Ni^0 and $Ni^{2+,surf}$ contents, which is subsequently investigated in detail.[57]

From the above results, the Quasi-MOF-9h catalyst exhibited the most excellent hydrogenation activity. Hence, a detailed investigation of reaction conditions (reaction temperature, reaction time and hydrogen pressure) was performed. The effect of reaction temperature on Quasi-MOF-9h was carried out under conditions of 3 MPa H_2 pressure for 4 h (Fig. 5a). The relatively low selectivity of THFA at below 60 °C could be explained by the low adsorption interaction between the intermediate FFA molecules and the active catalytic site at low temperatures. When the temperature varied from 50 °C to 70 °C, the conversion of FFR remained at a high level, but the selectivity of THFA increased remarkably from 58.1% to 98%, which showed that the temperature could dramatically affect the conversion of FFA to THFA. The conversion of FFR and the selectivity of THFA were almost unchanged upon further increasing the reaction temperature; therefore, 70 °C was chosen as the optimal reaction temperature. The effect of the reaction time was also investigated on the Quasi-MOF-9h catalyst. As shown in Fig. 5b, the conversion of FFR increased sharply to 98.2% within 90 min, which indicated that the high activity of the catalyst enabled the rapid transformation of FFR under mild conditions. It showed a good linear relationship between THFA selectivity and reaction time within 3 h, and the selectivity of THFA increased regularly from 24.8% to 92.6%. The above results indicated that the hydrogenation of FFR to THFA is a consecutive two-step sequential hydrogenation process in which the former is the hydrogenation of the aldehyde group outside the furan ring, and the latter is the hydrogenation of the furan ring. Among them, the hydrogenation of the furan ring is the rate-determining step of the whole hydrogenation process. Impressively, complete FFR conversion with high THFA selectivity of 98% was achieved when the reaction was carried out for up to 4 h. Besides, H_2 pressure is a pivotal indicator and the dependence on H_2 pressure was investigated at 70 °C within 4 h. As the H_2 pressure increased from 1.5 MPa to 3.5 MPa, the FFR conversion maintained near 100% (Fig. 5c), which implied that the adsorption and activation of –C═O were not affected by H_2 pressure under current conditions. In contrast, the THFA selectivity decreased significantly when the H_2 pressure was below 3 MPa, showing that the hydrogenation of the furan ring was highly dependent on H_2 pressure. In total, excellent catalytic performance with 100% FFR conversion and 98% THFA selectivity was achieved under 3 MPa initial H_2 pressure at 70 °C for 4 h. The catalytic performance of Quasi-MOF-9h ranks among the highest reported noble metal, non-noble metal and bimetallic catalysts (Table S6, ESI†).

With these optimal conditions, the stability of the Quasi-MOF-9h catalyst was examined (Fig. 5d). After the reaction, the catalyst was recovered by the centrifugation method, followed by washing with ethanol three times and drying overnight. The catalyst was used repeatedly for five runs and no significant loss of its conversion and selectivity was observed. The recycled catalysts were further characterized by XRD, N_2 adsorption–desorption isotherms and TEM analyses to understand the changes in the structure and surface information. XRD and N_2 adsorption results showed that the used Quasi-MOF-9h catalyst has non-obvious changes in the structure (Fig. S22 and S23, ESI†). Moreover, the TEM results showed no agglomeration of the Ni nanoparticles after continuous hydrogenation (Fig. S24, ESI†), which also proves that the strong interaction

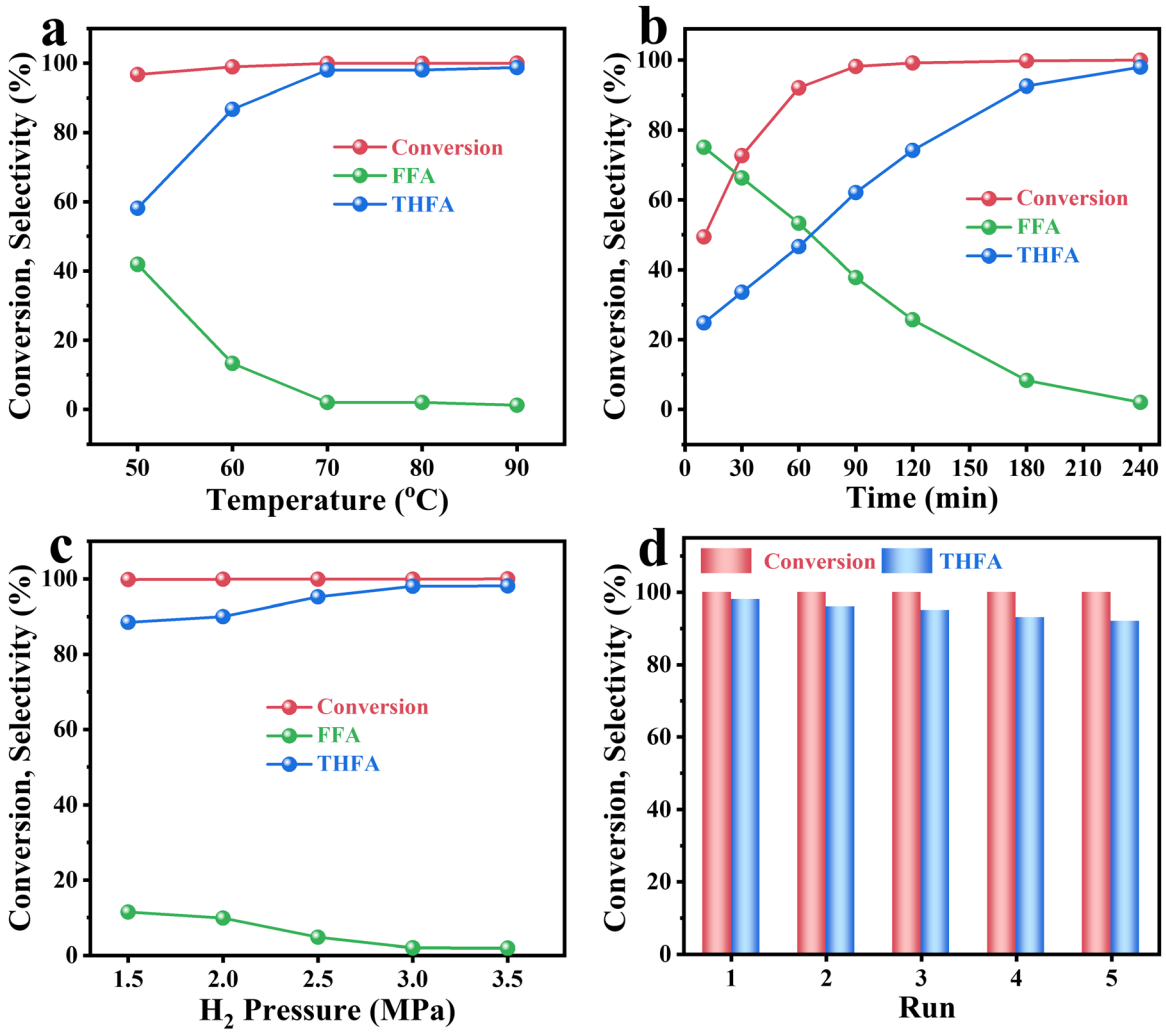

Fig. 5 (a) Effect of reaction temperatures (3 MPa H_2, 4 h), (b) effect of the reaction time (3 MPa H_2, 70 °C), (c) effect of H_2 pressure (70 °C, 4 h), (d) the reusability of the Quasi-MOF-9h catalyst (3 MPa H_2, 70 °C, 4 h), other reaction conditions: 0.6 g of FFR, 50 mL of ethanol, and 0.1 g of Quasi-MOF-9h.

between Quasi-MOF and metallic Ni hinders the aggregation of metal particles. These analysis results illustrated that the as-prepared Quasi-MOF-9h catalyst was efficient and robust for the hydrogenation reaction.

3.3. Investigations on the structure–activity relationship

According to the results mentioned above of structural features and catalytic performance, a linear relationship between the THFA yield and the percentage of (Ni^0 + $Ni^{2+,surf}$) was obtained (R^2 = 0.999) (Fig. 6a). Specifically, the THFA yields of Quasi-MOF samples give the following order: Quasi-MOF-9h (86.7%) > Quasi-MOF-6h (70.7%) > Quasi-MOF-3h (27.1%). The percentage of (Ni^0 + $Ni^{2+,surf}$), based on Ni 2p high-resolution spectra (Fig. 4a and Table S4, ESI†), displays the same sequence: Quasi-MOF-9h (42%) > Quasi-MOF-6h (41%) > Quasi-MOF-3h (39%). Although abundant surface NiO species existed in Ni/NiO/C-12h, the deficiency of metallic Ni gives it a less favorable hydrogenation activity, with a THFA yield of only 17.8%. Hence, the surface NiO species itself cannot improve the catalytic activity, and must be cooperated with metallic Ni to give enhanced catalytic activity. Meantime, the percentage of $Ni^{2+,surf}$ also correlated with the yield of THFA (Fig. S25, ESI†), which strongly suggests that the presence of surface NiO species in Quasi-MOF samples greatly facilitates the hydrogenation reaction of FFR. Furthermore, the total pore volume, reflecting the number of unique hub-and-spoke channels, displays the same linearly order: Quasi-MOF-9h (1.02 $cm^3\ g^{-1}$) > Quasi-MOF-6h (0.91 $cm^3\ g^{-1}$) > Quasi-MOF-3h (0.78 $cm^3\ g^{-1}$) > Ni/NiO/C-12h (0.54 $cm^3\ g^{-1}$) (Fig. S26, ESI†). The above result demonstrates that the total pore volume of the catalysts also correlates with FFR hydrogenation activity.

Hydrogen temperature-programmed desorption (H_2-TPD) analysis was performed to investigate the hydrogen adsorption ability of the Quasi-MOF samples (Fig. 6b). In the case of Quasi-MOFs, the bridge adsorption of H_2 molecules increases gradually with extending the heat treatment time, resulting from the increased amount of the reduced metal Ni sites.[55] The Quasi-MOF-9h sample exhibited the highest hydrogen adsorption

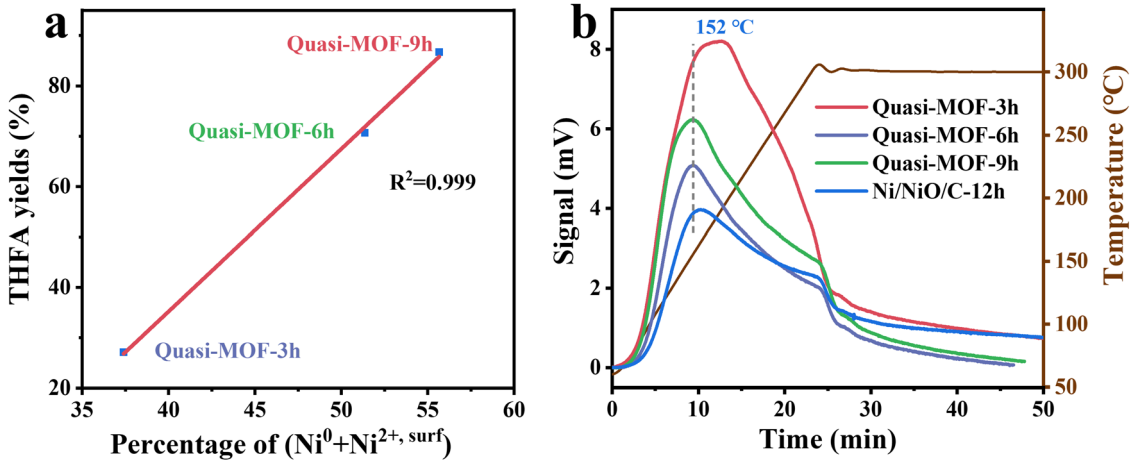

Fig. 6 (a) Correlation between percentage of (Ni^0 + $Ni^{2+,surf}$) and THFA yields; (b) H_2-TPD curves of the derivatives of Ni-MOF-74.

capacity, consistent with the FFR hydrogenation results (Fig. S27, ESI†). Additionally, a higher hydrogen desorption temperature was noticed for Ni-MOF-74 (350) samples (206 °C) compared to Quasi-MOF samples (150 °C) (Fig. S28, ESI†). This phenomenon points out that the interaction between surface NiO species in Quasi-MOFs and hydrogen is weak compared to that between pure metallic Ni and hydrogen. Therefore, the desorption of active H species is much easier on the Quasi-MOF samples with abundant surface NiO species, accelerating the subsequent hydrogenation steps.

3.4. Substrate scope

The hydrogenation of a series of substrates containing furan ring, nitryl and carbonyl groups was also explored to verify the applicability of the Quasi-MOF-9h catalyst. As displayed in Table 2, the Quasi-MOF-9h catalyst exhibited excellent adaptability for all the selected substrates under the examined mild conditions. In all cases, more than 95% of conversions are obtained, and the selectivity for target products exceeds 90%. The results further substantiate that the Quasi-MOF-9h catalyst featured with abundant Ni^0, surface NiO species and special hub-and-spoke channels can work as an efficient catalyst for the hydrogenation of unsaturated groups, reflecting its potential applications in the high-efficiency transformation and utilization of biomass-derived compounds.

Based on the above results, it is reasonable to believe that the surface NiO species in the Ni metal layer are deficient. Since the oxygen atoms in both the C═O group and furan ring of FFR are negatively charged, the surface NiO species in the Quasi-MOF samples can facilitate the adsorption of the C═O and furan ring to a large extent. Meanwhile, the hub-and-spoke channels can serve more exposed active sites and facilitate the mass transfer capability of the reactants to accelerate the hydrogenation reaction. As the Quasi-MOF samples showed enhanced H-donation capacity reflected in the lower hydrogen desorption temperature, the role of surface NiO species and Ni^0 can be to adsorb FFR molecules and dissociate hydrogen, respectively. Subsequently, the FFR molecules migrate and adsorb on adjacent Ni particles (Scheme 2). The released activated H species could attack the adsorbed unsaturated

Table 2 Hydrogenation performance of different substrates over the Quasi-MOF-9h catalyst

Entry	Substrate	Product	Conversion (%)	Selectivity (%)
1	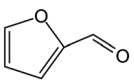	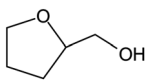	100	98.0
2	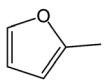	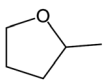	99.2	98.4
3	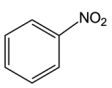	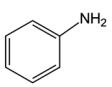	100	93.4
4	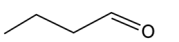	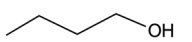	95.9	93.6
5	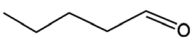	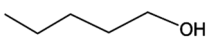	95.8	99.9
6	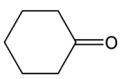	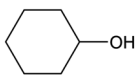	100	99.9

Reaction conditions: 0.6 g of substrate, 0.1 g of catalyst, 50 mL of ethanol, 70 °C, 3 MPa H_2 pressure, 4 h.

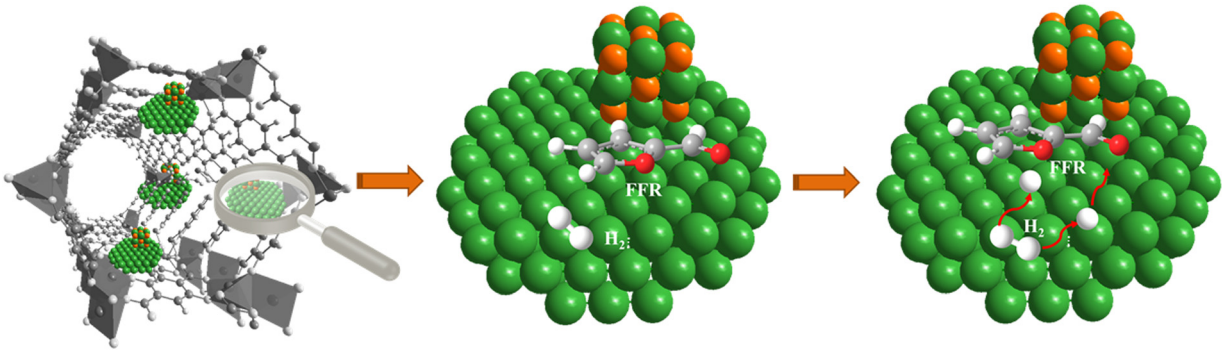

Scheme 2 Illustration of FFR molecule adsorption at Quasi-MOFs.

C═O and furan rings, thus, increasing the activity of the total hydrogenation of FFR molecules.

4. Conclusions

In this work, a novel catalyst, Quasi-MOF, was synthesized using a controlled partial thermal decomposition strategy. The unique hub-and-spoke channels as well as the interaction between the Ni^0 and surface NiO species are causalities for the excellent catalytic performance. The surface NiO species are beneficial for promoting the adsorption of electron enrichment groups in FFR. Among the as-prepared Quasi-MOF catalysts, the Quasi-MOF-9h catalyst displayed the best hydrogenation activity owing to the following three reasons: (i) the presence of high contents of surface NiO species enhances the affinity between active sites and FFR molecules; (ii) the synergistic effect between Ni and the Quasi-MOF framework suppresses the aggregation of metallic Ni; (iii) the unique hub-and-spoke channels increase the total pore volume and expose more catalytically active sites, which benefits the diffusion of the reactants and products. Notably, the Quasi-MOF-9h catalyst has durable cycle stability. Using Quasi-MOF-9h as the catalyst, the FFR was converted entirely and the selectivity of THFA reached 98% within 4 h at 70 °C and 3 MPa initial H_2 pressure, ranking it the best among the non-noble metal catalysts and even surpassing a few precious metal catalysts. This work highlights the unique properties of the quasi-MOF, and the strategy of Quasi-MOF synthesis can also be applied to design other non-noble efficient catalysts for upgrading bio-derived feedstocks.

Author contributions

Qiuju Fu: investigation and writing – original draft. Liting Yan: methodology and data curation. Lingzhi Yang: resources, and writing – review & editing. Dandan Liu: investigation. Shuo Zhang: software. Huimin Jiang: writing – original draft. Wenpeng Xie: formal Analysis. Haiyan Wang: supervision. Xuebo Zhao: conceptualization, funding acquisition, and writing – review & editing.

Conflicts of interest

There are no conflicts to declare.

Acknowledgements

This work was supported by the National Natural Science Foundation of China (Grant No. 52302271, 22205189 and 21975286), the China Postdoctoral Science Foundation (Grant No. 2022M723030), the Youth Innovation and Technology Support Plan of Shandong Province (Grant No. 2022KJ135), the Colleges and Universities Twenty Terms Foundation of Jinan City (Grant No. 202228053), and the QLUT Special Funding for Distinguished Scholars (Grant No. 2419010420).

References

1 S. Campisi, C. E. ChanThaw, L. E. Chinchilla, A. Chutia, G. A. Botton, K. M. H. Mohammed, N. Dimitratos, P. P. Wells and A. Villa, *ACS Catal.*, 2020, **10**, 5483–5492.
2 X. Li, P. Jia and T. Wang, *ACS Catal.*, 2016, **6**, 7621–7640.
3 R. Insyani, A. F. Barus, R. Gunawan, J. Park, G. T. Jaya, H. S. Cahyadi, M. G. Sibi, S. K. Kwak, D. Verma and J. Kim, *Appl. Catal., B*, 2021, **291**, 120120.
4 Y. Zhu, W. Zhao, J. Zhang, Z. An, X. Ma, Z. Zhang, Y. Jiang, L. Zheng, X. Shu, H. Song, X. Xiang and J. He, *ACS Catal.*, 2020, **10**, 8032–8041.
5 H. E. Hoydonckx, W. M. Van Rhijn, W. Van Rhijn, D. E. De Vos and P. A. Jacobs, *Ullmann's Encycl. Ind. Chem.*, 2007, **16**, 285–309.
6 R. Mariscal, P. MairelesTorres, M. Ojeda, I. Sádaba and M. López Granados, *Environ. Environ. Sci.*, 2016, **9**, 1144–1189.
7 J. Xu, Q. Cui, T. Xue, Y. Guan and P. Wu, *ACS Omega*, 2020, **5**, 30257–30266.
8 N. S. Date, A. M. Hengne, K. W. Huang, R. C. Chikate and C. V. Rode, *Green Chem.*, 2018, **20**, 2027–2037.
9 Z. Fan, W. Zhang, L. Li, Y. Wang, Y. Zou, S. Wang and Z. Chen, *Green Chem.*, 2022, **24**, 7818–7868.
10 J. Wu, G. Gao, J. Li, P. Sun, X. Long and F. Li, *Appl. Catal., B*, 2017, **203**, 227–236.

11 S. Pendem, S. R. Bolla, D. J. Morgan, D. B. Shinde, Z. Lai, L. Nakka and J. Mondal, *Dalton Trans.*, 2019, **48**, 8791–8802.
12 Q. Fu, H. Jiang, Y. Wang, H. Wang and X. Zhao, *Mater. Chem. Front.*, 2023, **7**, 628–642.
13 Y. Su, Z. Li, H. Zhou, S. Kang, Y. Zhang, C. Yu and G. Wang, *Chem. Eng. J.*, 2020, **402**, 126205.
14 L. Ruan, A. Pei, J. Liao, L. Zeng, G. Guo, K. Yang, Q. Zhou, N. Zhao, L. Zhu and B. H. Chen, *Fuel*, 2021, **284**, 119015.
15 F. Tang, L. Wang, M. Dessie Walle, A. Mustapha and Y. Liu, *J. Catal.*, 2020, **383**, 172–180.
16 Y. Yang, L. Chen, Y. Chen, W. Liu, H. Feng, B. Wang, X. Zhang and M. Wei, *Green Chem.*, 2019, **21**, 5352–5362.
17 Y. Cao, H. Zhang, K. Liu, Q. Zhang and K. Chen, *ACS Sustainable Chem. Eng.*, 2019, **7**, 12858–12866.
18 Z.-L. Wu, J. Wang, S. Wang, Y.-X. Zhang, G.-Y. Bai, L. Ricardez-Sandoval, G.-C. Wang and B. Zhao, *Green Chem.*, 2020, **22**, 1432–1442.
19 Y. Qian, Z.-J. Li, X.-L. Du, Q. Zhang, Y. Zhao, Y.-M. Liu and Y. Cao, *Green Chem.*, 2020, **22**, 850–859.
20 Y. Su, C. Chen, X. Zhu, Y. Zhang, W. Gong, H. Zhang, H. Zhao and G. Wang, *Dalton Trans.*, 2017, **46**, 6358–6365.
21 Y. Zhu, B. Li, Y. Fang and C. Zhao, *Green Chem.*, 2022, **24**, 5770–5778.
22 Q. Fu, W. Niu, L. Yan, W. Xie, H. Jiang, S. Zhang, L. Yang, Y. Wang, Y. Xing and X. Zhao, *Mater. Lett.*, 2023, **343**, 134344.
23 X. Zhao, B. Xiao, A. J. Fletcher, K. M. Thomas, D. Bradshaw and M. J. Rosseinsky, *Science*, 2004, **306**, 1012–1015.
24 L. Yang, L. Yan, Y. Wang, Z. Liu, J. He, Q. Fu, D. Liu, X. Gu, P. Dai, L. Li and X. Zhao, *Angew. Chem., Int. Ed.*, 2021, **60**, 4570–4574.
25 L. Yang, W. Xie, Q. Fu, L. Yan, S. Zhang, H. Jiang, L. Li, X. Gu, D. Liu, P. Dai, Q. Zheng, X. Zhao and A. Bonilla-Petriciolet, *Adsorpt. Sci. Technol.*, 2023, **2023**, 1–9.
26 L. Yang, L. Yan, W. Niu, Y. Feng, Q. Fu, S. Zhang, Y. Zhang, L. Li, X. Gu, P. Dai, D. Liu, Q. Zheng and X. Zhao, *Angew. Chem., Int. Ed.*, 2022, **61**, e202204046.
27 C. Guo, Y. Zhang, Y. Zhang and J. Wang, *Chem. Commun.*, 2018, **54**, 3701–3704.
28 A. H. Valekar, M. Lee, J. W. Yoon, J. Kwak, D. Hong, K. Oh, G. Cha, Y. Kwon, J. Jung, J. Chang and Y. K. Hwang, *ACS Catal.*, 2020, **10**, 3720–3732.
29 H. Wang, F. Yin, B. Chen, X. He, P. Lv, C. Ye and D. Liu, *Appl. Catal., B*, 2017, **205**, 55–67.
30 Q. Fu, D. Liu, W. Niu, S. Zhang, R. Chen, Y. Wang, P. Zhao, H. Jiang, Y. Zhao, L. Yang, L. Yan, H. Wang and X. Zhao, *Fuel*, 2022, **327**, 125085.
31 Y. Zhang, L. Jiao, W. Yang, C. Xie and H. L. Jiang, *Angew. Chem., Int. Ed.*, 2021, **60**, 7607–7611.
32 H. Ye, L. Li, D. Liu, Q. Fu, F. Zhang, P. Dai, X. Gu and X. Zhao, *ACS Appl. Mater. Interfaces*, 2020, **12**, 57847–57858.
33 L. Yan, Y. Xu, P. Chen, S. Zhang, H. Jiang, L. Yang, Y. Wang, L. Zhang, J. Shen, X. Zhao and L. Wang, *Adv. Mater.*, 2020, **32**, 2003313.
34 H. Jiang, L. Yan, S. Zhang, Y. Zhao, X. Yang, Y. Wang, J. Shen, X. Zhao and L. Wang, *Nano-Micro Lett.*, 2021, **13**, 215.
35 S. Zhang, P. Dai, H. Liu, L. Yan, H. Song, D. Liu and X. Zhao, *Electrochim. Acta*, 2021, **369**, 137681.
36 K. Chen, J. Ling and C. Wu, *Angew. Chem., Int. Ed.*, 2019, **58**, 2–9.
37 Q. Zhu, J. Li and Q. Xu, *J. Am. Chem. Soc.*, 2013, **135**, 10210–10213.
38 A. Aijaz, A. Karkamkar, Y. J. Choi, N. Tsumori, E. Ronnebro, T. Autrey, H. Shioyama and Q. Xu, *J. Am. Chem. Soc.*, 2012, **134**, 13926–13929.
39 K. Nakatsuka, T. Yoshii, Y. Kuwahara, K. Mori and H. Yamashita, *Chem. – Eur. J.*, 2017, **24**, 898–905.
40 L. Chen, H. Li, W. Zhan, Z. Cao, J. Chen, Q. Jiang, Y. Jiang, Z. Xie, Q. Kuang and L. Zheng, *ACS Appl. Mater. Interfaces*, 2016, **8**, 31059–31066.
41 L. Zou, C. Hou, Z. Liu, H. Pang and Q. Xu, *J. Am. Chem. Soc.*, 2018, **140**, 15393–15401.
42 B. N. Bhadra and S. H. Jhung, *Nanoscale*, 2018, **10**, 15035–15047.
43 B. Liu, W. Han, X. Li, L. Li, H. Tang, C. Lu, Y. Li and X. Li, *Appl. Catal., B*, 2019, **257**, 117939.
44 D. Luo, C. Li, Y. Zhang, Q. Ma, C. Ma, Y. Nie, M. Li, X. Weng, R. Huang, Y. Zhao, L. Shui, X. Wang and Z. Chen, *Adv. Mater.*, 2021, **34**, 2105541.
45 N. Tsumori, L. Chen, Q. Wang, Q.-L. Zhu, M. Kitta and Q. Xu, *Chem*, 2018, **4**, 845–856.
46 Y. Shen, L. Bao, F. Sun and T. Hu, *Mater. Chem. Front.*, 2019, **3**, 2363–2373.
47 P. Cao, L. Lin, H. Qi, R. Chen, Z. Wu, N. Li, T. Zhang and W. Luo, *ACS Catal.*, 2021, **11**, 10246–10256.
48 D. Liu, Q. Fu, C. Feng, T. Xiang, H. Ye, Y. Shi, L. Li, P. Dai, X. Gu and X. Zhao, *Nanomaterials*, 2023, **13**, 285.
49 F. Lan, H. Zhang, C. Zhao, Y. Shu, Q. Guan and W. Li, *ACS Catal.*, 2022, **12**, 5711–5725.
50 W. Cui, Y. Li, H. Zhang, Z. Wei, B. Gao, J. Dai and T. Hu, *Appl. Catal., B*, 2020, **278**, 119262.
51 D. Kim and A. Coskun, *Angew. Chem., Int. Ed.*, 2017, **56**, 5071–5076.
52 H. Zhao, X. Wang, J. Feng, Y. Chen, X. Yang, S. Gao and R. Cao, *Catal. Sci. Technol.*, 2018, **8**, 1288–1295.
53 S. Wen, X. Gu, X. Ding, L. Zhang, P. Dai, L. Li, D. Liu, W. Zhang, X. Zhao and Z. Guo, *Nano Res.*, 2021, **15**, 2083–2091.
54 Y. Ge, X. Qin, A. Li, Y. Deng, L. Lin, M. Zhang, Q. Yu, S. Li, M. Peng, Y. Xu, X. Zhao, M. Xu, W. Zhou, S. Yao and D. Ma, *J. Am. Chem. Soc.*, 2020, **143**, 628–633.
55 L. Soriano, I. Preda, A. Gutiérrez, S. Palacín, M. Abbate and A. Vollmer, *Phys. Rev. B: Condens. Matter Mater. Phys.*, 2007, **75**, 233417.
56 H. Cheng, X. Long, F. Bian, C. Yang, X. Liu and H. Jiang, *J. Catal.*, 2020, **389**, 121–131.
57 Q. Fu, L. Yan, D. Liu, S. Zhang, H. Jiang, W. Xie, L. Yang, Y. Wang, H. Wang and X. Zhao, *Appl. Catal., B*, 2024, **343**, 123501.